Imaging of Spatiotemporal Coincident States by DC Optical Tomography

Harry L. Graber*, Yaling Pei, and Randall L. Barbour

***Abstract*—The utility of optical tomography as a practical imaging modality has, thus far, been limited by its intrinsically low spatial resolution and quantitative accuracy. Recently, we have argued that a broad range of physiological phenomena might be accurately studied by adopting this technology to investigate dynamic states (Schmitz *et al.*, 2000; Barbour *et al.*, 2000; Graber *et al.*, 2000; Barbour *et al.*, 2001; and Barbour *et al.*, 1999). One such phenomenon holding considerable significance is the dynamics of the vasculature, which has been well characterized as being both spatially and temporally heterogeneous.**

In this paper, we have modeled such heterogeneity in the limiting case of spatiotemporal coincident behavior involving optical contrast features, in an effort to define the expected limits with which dynamic states can be characterized using two newly described reconstruction methods that evaluate normalized detector data: the normalized difference method (NDM) and the normalized constraint method (NCM). Influencing the design of these studies is the expectation that spatially coincident temporal variations in both the absorption and scattering properties of tissue can occur *in vivo*. We have also chosen to model dc illumination techniques, in recognition of their favorable performance and cost for practical systems. This choice was made with full knowledge of theoretical findings arguing that separation of the optical absorption and scattering coefficients under these conditions is not possible.

Results obtained show that the NDM algorithm provides for good spatial resolution and excellent characterization of the temporal behavior of optical properties but is subject to interparameter crosstalk. The NCM algorithm, while also providing excellent characterization of temporal behavior, provides for improved spatial resolution, as well as for improved separation of absorption and scattering coefficients. A discussion is provided to reconcile these findings with theoretical expectations.

***Index Terms*—Crosstalk and nonuniqueness, dynamic optical tomography, inverse problem, physiological dynamics, physiological oscillations.**

I. Introduction

ASSESSMENT of tissue function by noninvasive methods is playing an increasingly important role in the detection and management of disease processes. One class of measurements having clinical significance is the monitoring of hemoglobin states. These can be studied continuously and noninvasively with near infrared (NIR) optical methods [5]. Many groups are attempting to apply these methods in either nonimaging near infrared spectroscopic [6]–[10]; topographic imaging, [11]–[15]; or tomographic imaging [16]–[18] modes for the purpose of studying large tissue structures. While promising results are being reported, the practicality of these methods remains to be clearly defined. One concern is the spatial resolution, which most investigators report as being on the order of 0.5 cm at best [19]–[22]. How much of this is due to fundamental limits attributable to scattering, and how much to limits in methodology, is unclear. Regardless, given the resolution of alternative imaging methods, the practical utility of spatial maps having such resolution seems limited. It is our view, however, that the real value of imaging large tissue structures with NIR light lies in its having superior performance not in the spatial domain, but rather in the time domain.

Measures that provide information regarding the temporal properties of hemoglobin states in tissue (i.e., blood volume, blood oxygenation) are commonly performed and have substantial value. For thin structures (e.g., fingers), optical methods in the form of pulse oximetry [23] and photoplethysmography [24] are used to measure arterial oxygenation levels and blood volume changes, respectively. For large tissues, blood volume changes often are measured using pneumoplethysmographic methods in the form of pulse volume recording [25]. In each case, the methodology employed provides a spatially integrated, time-varying signal.

A key value of collecting time-series measurements using NIR optical methods is that one can isolate signals unique to the vascular compartment. Significantly, features of the vascular rhythms, which include the cardiac ($\sim$1 Hz–$\sim$2 Hz), respiratory ($\sim$0.1 Hz–$\sim$0.5 Hz), and vasomotor ($\sim$0.04 Hz–$\sim$0.15 Hz) frequency ranges, are known to reflect critical physiological functions and often serve as markers for disease. For instance, a reduced amplitude in the cardiac frequency band, when observed distal to areas having more normal values in pulse volume recordings, is a reliable indicator of arterial stenosis between the two measuring sites. In situations of this type, we believe that the ability to localize such events on the basis of their temporal signatures, without the need for contrast agents, and with the spatial resolution that is currently achievable by optical tomography, could have substantial practical value. In addition to pathologies associated with the principal arteries, it is likely that many other practical applications could be found from studies focused on the venous and microcirculatory compartments of the vascular tree. In fact, features attributable to the principal structures of the vascular tree are readily identifiable, as a consequence of their distinct temporal properties.

Manuscript received June 1, 2001; revised March 15, 2002. This work was supported by the National Institutes of Health (NIH) under Grant RO1-CA 66184 and Grant R21-HL67738702. The Associate Editor responsible for coordinating the review of this paper and recommending its publication was M. W. Vannier. *Asterisk indicates corresponding author*.

*H. L. Graber is with SUNY Downstate Medical Center, 450 Clarkson Avenue, Brooklyn, NY 11203 USA (e-mail: hgraber@downstate.edu)

Y. Pei is with NIRx Medical Technologies Corp., Glen Head, NY 11545 USA.

R. L. Barbour is with SUNY Downstate Medical Center, Brooklyn, NY 11203 USA.

Digital Object Identifier 10.1109/TMI.2002.801154

For instance, if a beat frequency detected in the periphery is equal to the rate of ventricular contraction, then it can be reliably taken as originating from arterial structures. Similar associations between the respiratory frequency and venous structures, and vasomotor frequencies and the microvessels, are well known [26].

The existence of distinct frequency ranges in the vascular response, the deep penetrating power of NIR photons, and the relative homogeneity of chromophores that absorb light at these wavelengths in tissue is a useful fortuitous combination. While the value of optical parameter maps may be limited as a consequence of their modest spatial resolution, it is our view that similar maps that encode temporal signatures, which serve to define distinct functional properties of the vasculature and its interaction with the surrounding tissues, will likely have substantial value. It is worth emphasizing that this information is obtainable without the use of contrast agents. The contrast mechanism is the natural temporal variability of the hemoglobin signal itself.

Recently, we have begun to explore this promising territory. Our approach comprises three principal efforts. First, we recognize the need to have available a well-engineered, yet flexible, data-collection platform suitable for examining the temporal variability of the vascular response in a large volume of tissue [1], [27], [28]. Second, we have sought to improve on the stability and speed of the numerical methods used for image reconstruction [29]–[31]. Third, we have focused our attention on characterizing the accuracy with which temporal information attributable to dynamic processes can be identified in reconstructed spatial maps obtained using the experimental and numerical methods we have developed [2]–[4].

One important class of dynamic tissue models we have considered exhibit spatiotemporally coincident behavior. This refers to states wherein two or more time-varying processes are occurring at the same time and location. Certainly, this is a condition that can be expected to occur in tissue. For instance, temporal fluctuations in tissue blood volume at any one site need not parallel that of blood oxygenation. Similarly, the variability in the tissue optical absorption coefficient need not follow changes in light scattering.

In this paper, we have explored our ability to accurately characterize complex dynamic behavior in dense scattering media as a model of tissue, in the limiting case in which two different processes are spatially and temporally coincident. In particular, we have sought a further test of the fidelity with which two recently reported methods applied to dc data can simultaneously distinguish perturbations in absorption and diffusion coefficients when both exhibit different complex temporally varying behaviors at the same location [29]–[31]. Our test model considered two included objects, each of which has two distinct complex time-varying functions assigned to it, one corresponding to its absorption coefficient and the other to its scattering coefficient. Results obtained add to the accumulating evidence that dc optical tomography is capable of accurately characterizing complex dynamic states in highly scattering media.

II. Methods

Recent reports [3], [29] have described a new method for image recovery that is well suited for the analysis of time-series data, and which we have called the normalized difference method (NDM) [29]. Comparisons between first-order solutions obtained using this method and either the standard Born or Rytov approximation revealed that the NDM is remarkably stable to the image-degrading effects of an insufficiently accurate initial guess. This was revealed both by the qualitative accuracy of recovered spatial maps and by the fidelity of the recovered temporal behavior.

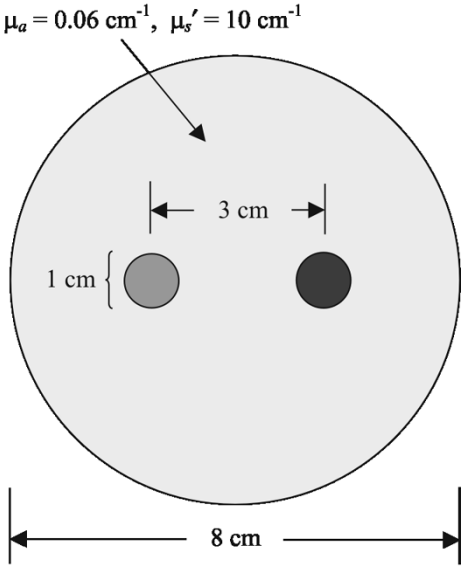

Fig. 1. Dimensions and geometry of target medium.

Building on the success obtained with the NDM, a modified algorithm, which we have called the normalized constraint method (NCM) [30], [31] was subsequently developed that retains the NDM's insensitivity to systematic error in the initial guess and also provides for improved separation of the absorption and scattering properties in the case of dc measurements.

For this paper, our goal has been to quantify the fidelity with which both the NDM and NCM can isolate fluctuations in a medium's optical parameters, in the limiting case of spatiotemporally coincident behavior. Our basic approach has been to assign different time-varying functions to the absorption and scattering (diffusion) coefficients for two inclusions, compute the image time series, and compare the accuracy of the recovered spatial and temporal information.

A. Spatiotemporal Properties of Target Medium

The target medium explored, shown in Fig. 1, is a geometrically simple two-dimensional structure consisting of an 8-cm circle with two embedded 1-cm diameter inclusions. The absorption (μ_a) and reduced scattering (μ_s') coefficients of the light gray background in the figure were static, with numerical values of $\mu_a = 0.06$ cm^{-1} and $\mu_s' = 10$ cm^{-1}. Four time-varying functions—$\mu_a(L, t)$, $\mu_s'(L, t)$, $\mu_a(R, t)$, and $\mu_s'(R, t)$, where L and R, respectively, denote the left-hand (dark gray region in Fig. 1) and right-hand (black region in Fig. 1)—were assigned to the optical coefficients in the inclusions. That is, four different aperiodic fluctuations were present in the medium simultaneously, with two of the four spatially coincident in each inclusion.

TABLE I
PROPERTIES OF TEMPORAL FLUCTUATIONS ASSIGNED TO INCLUSIONS' OPTICAL COEFFICIENTS

μ_a			μ_s'		
Range (cm^{-1})	Dynamics		Range (cm^{-1})	Dynamics	
	Left	Right		Left	Right
0.096 – 0.144 (0.06 in background)	Quasiperiodic	Chaotic	12 – 18 (10 in background)	Chaotic	Stochastic

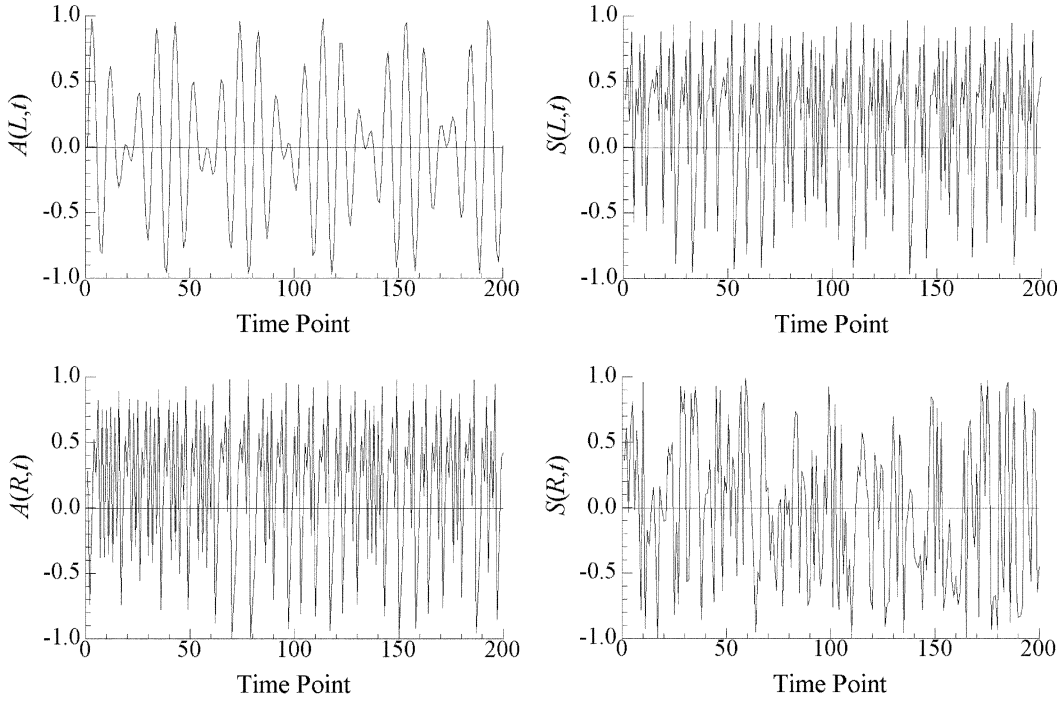

Fig. 2. Time series (rescaled to range from -1 to $+1$) assigned to the optical coefficients of the target medium's inclusions.

The particular functions chosen were easily generated representations of the types of dynamics that are known to occur in tissue vascular structures—quasi-periodic, chaotic, and stochastic fluctuations [32]. The ranges of coefficient values and the types of temporal fluctuation modeled are specified in Table I; the indicated ranges for μ_a and μ_s' represent 20% fluctuations about mean values of 0.12 and 15 cm^{-1}, respectively. The optical coefficient values assigned to the inclusions were computed from the formulas

$$\begin{aligned}\mu_a(L,\,t) &= 0.12[1 + 0.2A(L,\,t)]\\ \mu_a(R,\,t) &= 0.12[1 + 0.2A(R,\,t)]\\ \mu_s'(L,\,t) &= 15.0[1 + 0.2S(L,\,t)]\\ \mu_s'(R,\,t) &= 15.0[1 + 0.2S(R,\,t)] \qquad (1)\end{aligned}$$

where $A(L,\,t)$ is a quasi-periodic time series, $A(R,\,t)$ and $S(L,\,t)$ are chaotic time series and $S(R,\,t)$ is a stochastic time series, and the range of each of these four functions includes all values from -1 to $+1$. Plots showing the first 200 points of $A(L,\,t)$, $A(R,\,t)$, $S(L,\,t)$ and $S(R,\,t)$ are shown in Fig. 2. The quasi-periodic time series $A(L,\,t)$ was generated by adding two sinusoidal functions with incommensurate frequencies [33]. Chaotic time series $S(L,\,t)$ and $A(R,\,t)$ were generated by assigning randomly generated initial values to the Hénon equation [34]. While the same equation was used for both time series, by choosing different initial values the two chaotic time series generated are uncorrelated. The stochastic time series $S(R,\,t)$ was generated by drawing independent samples from a random variable uniformly distributed between -1 and $+1$. A total of 1000 values were computed for each function.

B. Detector Data Generation

Tomographic data for the simulated tissue models were acquired by using the finite element method to solve the diffu-

sion equation with Dirichlet boundary conditions for a dc source [29]–[31]. For a spatial domain Λ with boundary $\partial\Lambda$, this is represented by the expression

$$\nabla \cdot [D(\mathbf{r})\nabla\phi(\mathbf{r})] - \mu_a(\mathbf{r})\phi(\mathbf{r}) = -\delta(\mathbf{r}-\mathbf{r}_s), \qquad \mathbf{r} \in \Lambda \quad (2)$$

where $\phi(\mathbf{r})$ is the photon intensity at position $\mathbf{r}$, $\mathbf{r}_s$ is the position of a dc point source, and $D(\mathbf{r})$ and $\mu_a(\mathbf{r})$ are the position-dependent diffusion and absorption coefficients, respectively. Here, the definition used for the diffusion coefficient was $D(\mathbf{r}) = 1/\{3[\mu_a(\mathbf{r}) + \mu_s'(\mathbf{r})]\}$, where $\mu_s'(\mathbf{r})$ is the position-dependent reduced scattering coefficient. Forward-problem solutions were computed for each of six sources positioned about the target at 60° intervals, with each source located at a depth of 2 mm in from the extended boundary (i.e., within the strip lying between the physical and extended boundaries) [29]–[31]. Intensity values at eighteen locations, at the same depth as the sources but spaced at 20° intervals, were used as detector readings. Imaging operators were computed, in the manner described in [35], for each of the resulting 108 source/detector pairs. Sets of detector readings were computed for each value of the time-varying optical coefficients in the target's inclusions. A single set of imaging operators, computed for an 8-cm-diameter homogeneous medium whose properties are equal to those of the static region of the target, was used for all inverse problem computations.

C. Image Reconstruction Procedures

Both reconstruction algorithms considered in this paper seek to solve a modified perturbation equation whose form is

$$\mathbf{W}_r \cdot \delta\mathbf{x} = \delta\mathbf{I}_r \quad (3)$$

where $\delta\mathbf{x}$ is the vector of differences between the optical properties [e.g., absorption and scattering (diffusion) coefficients] of a target (measured) and a "background" medium, $\mathbf{W}_r$ is the weight matrix describing the influence that each voxel or element has on the surface detectors for the selected reference medium, and $\delta\mathbf{I}_r$ represents a normalized difference between detector readings obtained from the target in two distinct states. The difference between (3) and a standard linear perturbation equation lies in the structure of the right-hand side. In both the NDM and the NCM, the right-hand side of (3) is defined by

$$(\delta\mathbf{I}_r)_i = \frac{(\mathbf{I}-\mathbf{I}_0)_i}{(\mathbf{I}_0)_i}\,(\mathbf{I}_r)_i \quad (4)$$

where $\mathbf{I}_r$ is the computed detector readings corresponding to a selected reference medium, and $\mathbf{I}$ and $\mathbf{I}_0$ represent, in the examples considered here, the intensity at a specific time point and the time averaged mean, respectively. As explained in [29], formal solution of (3) gives $\delta\mathbf{x}$ as a sum of two terms. The first term is the conventional first-order perturbation equation solution. The second is a correction factor whose magnitude is a function of the difference between the properties of the media represented by the subscripts "r" and "0."

The NCM employs the same normalized difference [see (4)] in the right-hand side of (3) as the NDM does, and introduces two additional refinements [30], [31]. The first of these is weight-matrix scaling, in which the elements in each column of $\mathbf{W}_r$ are divided by that column's mean value. In the resulting system $\mathbf{W}_r' \cdot \delta\mathbf{x}' = \delta\mathbf{I}_r$, the scaled matrix $\mathbf{W}_r'$ is more uniform than $\mathbf{W}_r$ and has a lower condition number. The second refinement is to apply a range constraint to the image reconstruction, within each iteration.[1]

Here, reconstructions were carried out on the detector data time series using both the NDM and the NCM. We did so to provide a clear comparison of the quantitative differences and image quality derived, with particular, but not exclusive, emphasis on the issue of parameter isolation. In both cases, a conjugate gradient descent (CGD) algorithm [36] was used to compute numerical solutions to the modified perturbation equation [see (3)]. The reconstructions were carried out on a finite-element mesh containing 959 elements and 510 nodes (hence, 1020 unknowns); the same mesh was used at all time points and for both methods. For the NCM reconstructions we made appropriate use of prior knowledge of the algebraic signs of the perturbations. This involved applying a positivity constraint (i.e., lower bound zero, no upper bound) on the absorption coefficient and a negativity constraint (i.e., upper bound zero, no lower bound) on the diffusion coefficient.[2]

The (subsequently modified) procedure used for generating the data considered in this paper combined the forward- and inverse-problem computations in a single program, computing the detector data and reconstructed images for the first time point, then those for the second time point, etc. From the total elapsed time between successive image file writes, an upper limit of 2 min can be established for the image reconstruction time.

D. Quantitative Assessment of Temporal Accuracy and Interparameter Crosstalk

An important goal in developing post-reconstruction analysis schemes for image time series is the development of simple numerical indexes of the accuracy with which spatial and temporal features of the target medium are recovered. At the same time, it is recognized that any reduction of a large quantity of data into a single number entails the loss of information. The compromise we have struck is to select a set of six accuracy features whose numerical value can be precisely defined. These are: 1) qualitative spatial accuracy of the instantaneous or static image features; 2) quantitative accuracy of the instantaneous or static image features; 3) temporal fidelity; 4) interparameter crosstalk; 5) qualitative spatial accuracy of the temporal variability of the optical properties; and 6) quantitative accuracy of the temporal variability of the optical properties (see Tables II and III). Hereafter, we use the generic symbol u to stand for any of the modeled time-varying behaviors, and v to denote the time series of one of the recovered coefficients. Additionally, pairing of u and v in a subscript (e.g., r_{uv}) indicates comparison between a recovered optical coefficient and the corresponding coefficient in the target (e.g., target D versus image

[1]A consequence of the imposition of range constraints is that (3) becomes nonlinear with respect to the measurement data. That is, it is no longer the case that $\mathbf{W}_r^{-1}[a\delta\mathbf{I}_r^{(1)} + b\delta\mathbf{I}_r^{(2)}] = a\mathbf{W}_r^{-1}\delta\mathbf{I}_r^{(1)} + b\mathbf{W}_r^{-1}\delta\mathbf{I}_r^{(2)}$. As our reconstruction strategy does not, either explicitly or implicitly, depend on an assumption of this sort of linearity, no difficulty arises from its loss.

[2]Prior knowledge of the direction of perturbations with respect to the background is not, however, a requirement for implementation of the NCM. An example of successful recovery of properties of a target in which simultaneous positive and negative perturbations were present in both optical coefficients is presented in [31].

TABLE II
OPERATIONAL DEFINITIONS OF THE SPATIAL AND TEMPORAL ACCURACY FEATURES USED TO ASSESS AND COMPARE THE PERFORMANCE OF THE TWO IMAGE RECONSTRUCTION ALGORITHMS

Input Information Type	Spatial or Temporal Accuracy Feature	Operational Definition	Ideal Value
Static (Individual images)	Qualitative spatial accuracy of optical parameter values	$r_{uv}(t)$, $r_{u'v}(t)$; $u = u(x,y)$, $u' = u'(x,y)$, $v = v(x,y)$	$r_{uv}(t) = 1$, $r_{u'v}(t) = -1$[a]
	Quantitative accuracy (global)	$\frac{\delta_{uv}(t)}{s_u(t)}$	0
Dynamic (Image time series)	Temporal fidelity	$100 r^2_{(u\&u')v}(x,y)$; $u = u(t)$, $u' = u'(t)$, $v = v(t)$	100
	Inter–parameter crosstalk	$100 r^2_{u'v}(x,y)$[b]	0
	Qualitative spatial accuracy of temporal information	1) $s^*_{uv}(x,y)$[c], 2) $r_{u^*v^*}$; $u^* = s^*_{uu}(x,y)$, $v^* = s^*_{uv}(x,y)$	1) N/A[d], 2) 1
	Quantitative temporal accuracy	$\frac{\delta_{uv}(x,y)}{s(x,y)}$	0

Symbols used here denote: r_{uv} = correlation coefficient (see Table III); s_{uv} = covariance (see Table III); s^*_{uv} = standardized covariance (see Table III); δ_{uv} = root mean squared difference (see Table III); x, y = spatial coordinates; t = time; u, u' = either μ_a^m or D^m (m = model function, or target medium); v = either μ_a^i or D^i (i = image). a) This correlation is ideally -1 for the particular target medium considered in this report (because the absorption and diffusion coefficient perturbations are spatially coincident and have opposite algebraic signs), but not generally. b) If v designates, say, μ_a^i in a pixel within the left-hand inclusion, then u' can be any of the three modeled functions $D(L)^m$, $\mu_a(R)^m$, or $D(R)^m$. c) Here, u may designate any of the four modeled time-varying functions (as in Figs. 7 and 8). d) The qualitative spatial accuracy information resides in the appearance of the covariance map (see Figs. 7 and 8), rather than in the numerical values that are computed.

D), while pairing of u' and v in a subscript (e.g., $r_{u'v}$) indicates comparison between noncorresponding coefficients (e.g., target μ_a versus image D) Finally, the superscripts "i" and "m" are used, where necessary to remove ambiguity, to indicate optical parameter time series in the recovered images and in the target medium, respectively.

The first two of the six accuracy features are well appreciated and are applicable as well to phantom study results obtained for static imaging modalities. They identify the accuracy with which the recovered contrast features, for any given image within the time series, lie within the true boundaries of the corresponding target features and match the true inclusion contrast. As a quantitative index of spatial accuracy (first feature), we compute the spatial correlation r_{uv} between each recovered image in the time series and the true distribution of the corresponding optical parameter of the target medium at that instant (i.e. image μ_a versus target μ_a, image D versus target D). For the particular target medium we used, it was also useful to compute $r_{u'v}$, the spatial correlation between image μ_a and target D or between image D and target μ_a. Because all parameter perturbations were localized to the same two inclusions and $\Delta\mu_a$ was always positive while ΔD was always negative (relative to the background), these latter correlations ideally would be -1.

The spatial quantitative accuracy index (second feature) we have adopted is δ_{uv}/s_u, the ratio of the root mean squared (RMS) difference between the spatial distributions of an optical parameter of the target medium and image to the instantaneous standard deviation of the same parameter's spatial distribution in the target. The ideal value of the ratio is zero, because $\delta_{uv} = 0$ in a perfect reconstruction. A ratio of unity would indicate that, in quantitative terms, the reconstructed image is no better than a homogeneous spatial distribution equal to the mean of the optical parameter's true value in the target medium. A ratio greater than unity would indicate that the image is a quantitatively poorer representation of the target than the uniform target mean.

TABLE III
FORMULAS FOR COMPUTING INDICES OF SIMILARITY BETWEEN A SPATIALLY OR TEMPORALLY VARYING PROPERTY OF THE TARGET MEDIUM (u) AND OF THE SET OF RECONSTRUCTED IMAGES (v)

Statistical Similarity Index	Formula
Covariance (s_{uv})	$s_{uv} = \frac{1}{N-1}\sum_{n=1}^{N}(u_n - \bar{u})(v_n - \bar{v})$
Standardized Covariance (s^*_{uv})	$s^*_{uv} = \frac{1}{N-1}\sum_{n=1}^{N}\left(\frac{u_n - \bar{u}}{s_u}\right)(v_n - \bar{v})$
Correlation Coefficient (r_{uv})	$r_{uv} = \frac{1}{N-1}\sum_{n=1}^{N}\left(\frac{u_n - \bar{u}}{s_u}\right)\left(\frac{v_n - \bar{v}}{s_v}\right)$
Root Mean Squared Difference (δ_{uv})	$\delta_{uv} = \left[\frac{1}{N}\sum_{n=1}^{N}(u_n - v_n)^2\right]^{1/2}$

Here, $\bar{u}$ and $\bar{v}$ are the mean values of u and v, s_u and s_v are their standard deviations, and N is the number of pixels (spatial similarity) or of time points (temporal similarity) included in the calculation. When computing first and second accuracy features (see Table II), indicated summations are performed over all spatial locations, for a fixed time point. For the third through sixth features, summations are over all time points at a fixed position.

The temporal fidelity (third feature) of a time series is measured by the accuracy with which the image time series recovers the true local temporal variations of the target medium. We consider perfect temporal fidelity to occur when the recovered time series for either optical coefficient is equal to any linear combination of the true temporal functions in both optical coefficients at the same location. We adopt this definition to allow for a clear distinction between temporal fidelity and crosstalk.[3] The corresponding quantitative index is (see Table II) $100r^2_{(u\&u')v}$, the square of the correlation coefficient (expressed as a percentage) obtained from a linear fitting of the single recovered time series v to the two target medium time series u and u' at the same location. The numerical value obtained is the percentage of the total temporal variability in v that is linearly attributable to the temporal variability in the optical parameters of the medium.

The issue of interparameter crosstalk (fourth accuracy feature) is relevant in cases where both coefficients are simultaneously recovered. In keeping with standard practice, we define crosstalk as the degree to which variations in one parameter are misrepresented as variations in the other in the recovered images. We note that in the case of spatially coincident μ_a and D, it can be difficult to distinguish quantitative errors originating from crosstalk from other factors that can influence the recovered coefficient values. Such discrimination, however, is possible in cases where an additional dimension of information exists, such as temporal variability associated with the inclusion contrast. The numerical index we use to measure crosstalk is the square of the correlation between a recovered optical parameter time series and the time series for the noncorresponding parameter of the medium at the same location, expressed as a percentage, or $100r^2_{u'v}$. [4] Ideally, this index would have a value of 0% at all points within the image.[5]

To assess the qualitative accuracy with which the recovered temporal behaviors coincide with the actual target locations (fifth feature), spatial maps of covariance (s_{uv}) values between the modeled functions and the recovered pixel time series were computed. Covariance is the appropriate measure of the degree to which a recovered temporal behavior is spatially accurate because, unlike the correlation, the (magnitude of the) covariance between two time-varying functions is large only if both functions evolve similarly in time and they both have large-amplitude fluctuations. For these computations, the ideal result would be that, say, the reconstructed $\mu_a(t)$ in pixels lying within the left- and right-hand inclusions, and only these pixels, show significant covariance with $\mu_a(L, t)$ and $\mu_a(R, t)$, respectively. At the same time, the reconstructed $\mu_a(t)$ should not significantly co-vary with either $D(L, t)$ or $D(R, t)$, in any region of the reconstructed images. Each computed covariance map was subsequently adjusted by dividing s_{uv} in each pixel by s_u, the standard deviation of the modeled function. The advantage of working with this ratio, which we refer to as the "standardized covariance" (s^*_{uv}), is that it simplifies the task of quantitatively comparing the results obtained for two or more modeled time-varying functions that have different variances.

The temporal quantitative accuracy index (sixth feature) is analogous to the second. In this case, we compute—at each spatial location within the inclusions—the ratio of the RMS difference between the temporal distributions of an optical parameter in the target medium and image to the standard deviation of the same parameter's temporal distribution at the same location in the target. The ideal value of this ratio is zero, while values

[3]It might be objected that it would be more sensible or intuitive to define temporal fidelity solely in terms of the relation between the dynamics of a recovered coefficient and of the corresponding coefficient in the target medium. In that case, however, there would not be a unique interpretation available for a finding of low temporal fidelity. Such a result could be the consequence of either an outright failure of the imaging process to capture the true patterns of temporal fluctuations within the target medium, or of a high level of inter-parameter crosstalk.

[4]Our use of temporal information to quantify crosstalk is the reason why this feature is included in the "Dynamic" classification in Table II, even though the occurrence of crosstalk is an issue that arises in all optical tomography domains, not exclusively in dynamic imaging

[5]The four time-varying functions assigned to the optical properties of the medium are mutually orthogonal; if this were not so, then of the ideal value for this index would be the corresponding value of the projection of u' onto u (see [36]).

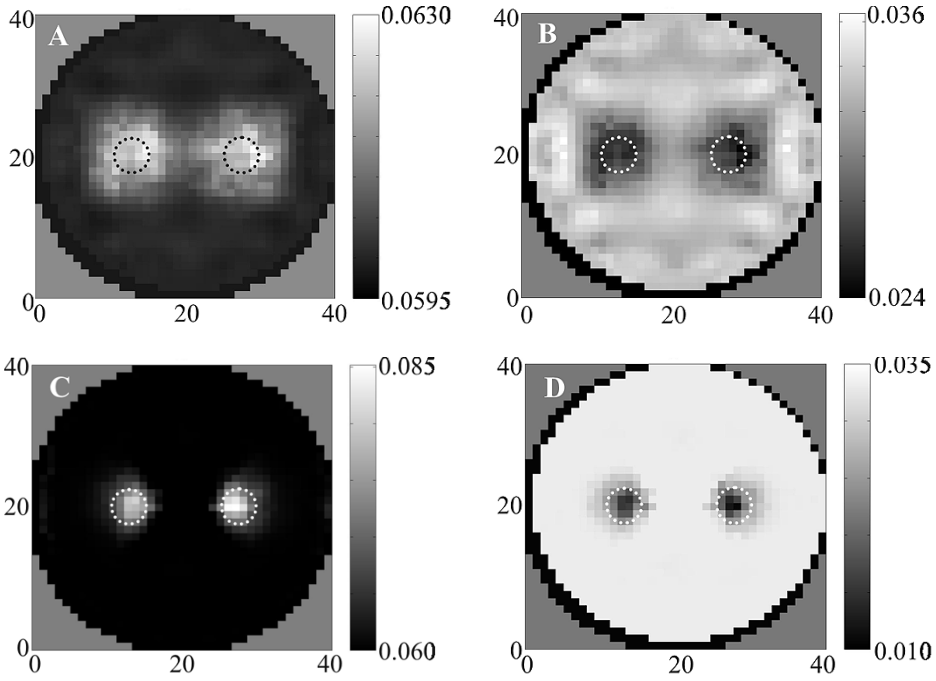

Fig. 3. Temporal averages, calculated over the complete set of 1000 reconstructed images in each time series, of μ_a [(A) and (C)] and of D [(B) and (D)] in the dynamic target medium sketched in Fig. 1. Results in (A) and (B) were obtained when the NDM was used for reconstruction, while those in (C) and (D) were obtained when the NCM was used instead.

greater than or equal to unity have interpretations analogous to those for the quantitative spatial accuracy index.

We wish to point out that we are aware that, whereas the accuracy features identified here are both informative and appropriate for the cases we are studying, it is not the case that they can be applied indiscriminately. More generally, assessment of image accuracy may require measures that seek to quantify local accuracy as well.

III. Results

A. Qualitative Spatial Accuracy of Optical Parameter Values

Examples of the recovered optical parameter images obtained using the two algorithms are shown in Fig. 3. The top row corresponds to the temporal mean value of the results obtained when the NDM was used, and the bottom row is the corresponding result obtained with the NCM. The dotted circles in these figures show the actual locations of the inclusions. Inspection reveals that the NCM provides a considerably more accurate spatial result, (i.e., improved edge detection and nearly free of artifact).

Calculation of the first accuracy index (Section II-D and Table II) produces the time series of spatial correlations that are shown in Fig. 4. As indicated in Table II, the ideal result for this computation is $r_{uv}(t) = 1$ and $r_{u'v}(t) = -1$. When the image time series whose temporal means are shown in Fig. 3 are compared to $\mu_a^m(t)$, the NDM images yield $r_{uv}(t)$ and $r_{u'v}(t)$ values whose means and CVs are 0.56, 1.4% and -0.58, 1.2%, respectively. The corresponding values for the NCM are 0.82, 1.9% and -0.84, 1.9%. This indicates that the NCM provides a considerably more spatially accurate result for each set of detector data within the time series.

The variability of the r_{uv}-versus-time and $r_{u'v}$-versus-time curves in Fig. 4 (among the eight functions plotted, the lowest CV is 0.6% and the highest is 3.9%) is an indication of the dependence of the spatial correlations on the temporal variability of the optical coefficients in the inclusions. It is seen that the spatial correlations exhibit no low-frequency fluctuations, which is significant because solutions to the forward problem certainly are nonlinear functions of the medium's optical coefficients. Consequently, it might have been anticipated *a priori* that there would be a nonlinear dependence of the recovered images on the assigned optical parameters as a function of time. Also, it might have been anticipated that the susceptibility of the reconstruction algorithm to the nonuniqueness phenomenon described by Arridge and Lionheart [37] would be a function of the time-varying optical coefficients values in the medium. It is evident, however, that neither of these possibilities is manifested in our result.

The spatial correlation data, while informative, do not completely characterize the accuracy of the reconstruction result, because they don't allow us to determine whether and to what extent there is interparameter crosstalk in a medium whose absorption and diffusion coefficients are spatially coincident. They also do not speak directly to the issue of the temporal fidelity of the recovered time series. Instead, these findings primarily address the question of whether and to what extent varying the magnitude of the optical coefficient perturbations in the medium affects the spatial accuracy of the recovered image.

B. Quantitative Accuracy of Static Optical Parameter Images

Calculation of the quantitative spatial accuracy index described in Methods produces a set of curves qualitatively similar to those in Fig. 4. Because of space limitations these

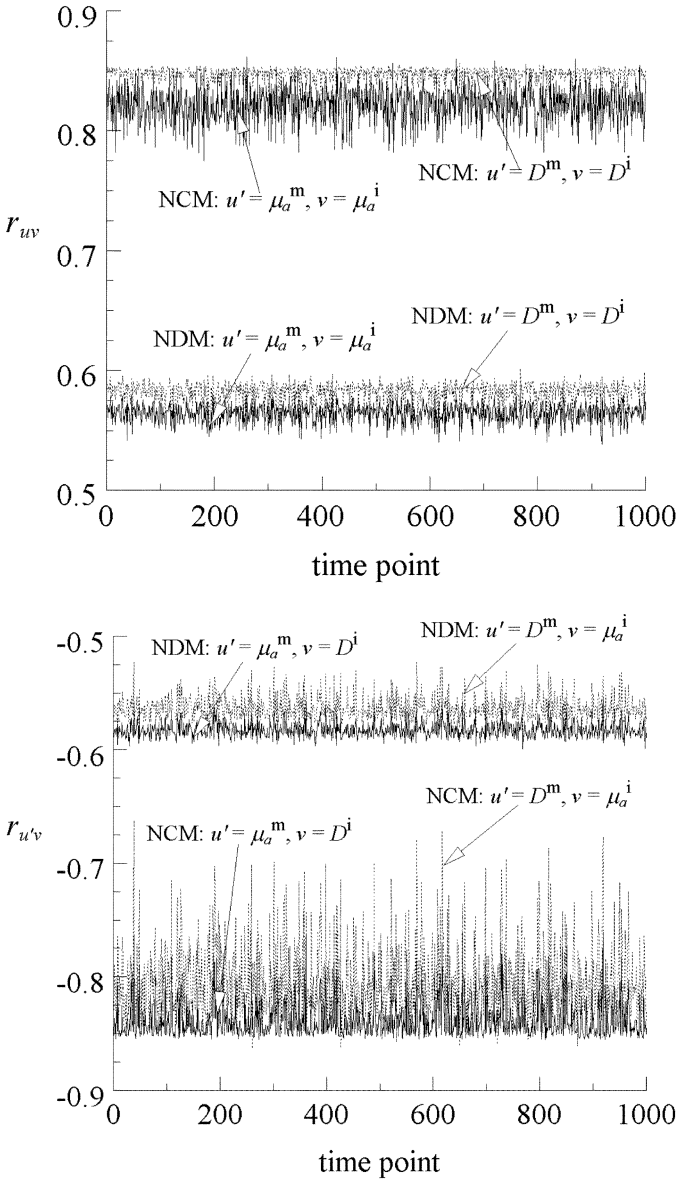

Fig. 4. Time-dependent correlations, for both NDM and NCM, between the spatial distribution of optical coefficients present in the target medium and in the reconstructed images.

are not reproduced here, and instead we briefly summarize them. The mean value and CV for images of μ_a reconstructed by the NDM are 0.99 and 0.37%, while for μ_a reconstructed by the NCM the corresponding numbers are 0.82 and 1.22%. These numbers show that there is an increase in quantitative accuracy of the NCM images relative to the NDM results. The mean value and CV obtained for the recovered images of D are 0.90, 6.10% for the NDM, and 0.62, 6.74% for the NCM, again revealing an increase in quantitative accuracy in the results produced by the latter. It is noteworthy that, for each reconstruction method, the D images have, on average, higher qualitative spatial accuracy than the μ_a images (see Fig. 4 and Table IV), but the D image time series also has greater temporal variability for the quantitative accuracy index. These findings suggest the possibility that, for both algorithms, increases in spatial resolution occur at the cost of larger confidence intervals for the recovered parameter values.

The quantitative accuracy that we compute is a global index, as the summation (Table III) performed to obtain the RMS difference is carried out over all pixels of the image. The quantitative accuracy achieved specifically for the optical parameters of the inclusions (i.e., local quantitative accuracy) is revealed by examination of the scales in Fig. 3. Note that results shown include the value of the background, and that the true temporal mean value for μ_a and D in the inclusions are 0.12 cm^{-1} and 0.022 cm, respectively. In the case of the NDM, we find that the μ_a contrast is grossly underestimated, while the recovered D is much closer to the true value. In the case of the NCM, we observe improved accuracy in the μ_a contrast, but this seemingly occurs at the expense of an overestimation of D contrast.

C. Temporal Fidelity

Shown in Fig. 5 are scatterplots wherein, for each of the two pixels considered in this example, the reconstructed $\mu_a(t)$ is plotted against the modeled $\mu_a(t)$ and $D(t)$. Each point in these scatterplots corresponds to one point in the time series. It is observed that the plotted points are nearly confined to a plane, two edges of which have been highlighted. The numerical values of the temporal fidelity index for the specific pixels considered in this figure are $100r^2_{(u\&u')v}(L) = 99.5\%$, $100r^2_{(u\&u')v}(R) = 98.6\%$. These results indicate that essentially all of the variability in $\mu_a(t)^i$ is attributable to a linear combination of $\mu_a(t)^m$ and $D(t)^m$. Thus, we find that whereas the surface detector responses vary nonlinearly with the assigned temporally varying optical coefficients, the reconstructed coefficients do not. This is by no means an inevitable result.

More extensive analysis of the data in Fig. 5 shows that they exhibit neither significant nonlinearity in the dependence of $\mu_a(t)^i$ on $\mu_a(t)^m$ and $D(t)^m$ nor any dependence of $\mu_a(t)^i$ on the remaining two modeled optical coefficients (i.e., absorption and diffusion coefficients in the other inclusion).

The same correlation analyses were applied to the time series of μ_a images reconstructed by the NCM algorithm. In Fig. 6, we show $\mu_a(t)^i$ versus $\mu_a(t)^m$ versus $D(t)^m$ scatterplots, for the same two pixels as in Fig. 5, but using the results produced by the NCM. The numerical values of the temporal fidelity indexes are $100r^2_{(u\&u')v}(L) = 99.4\%$, $100r^2_{(u\&u')v}(R) = 99.6\%$, which indicates that the use of constraints and weight-matrix scaling in the NCM does not result in any loss of temporal fidelity. It is again seen that each set of points defines a plane, two edges of which are highlighted. Note that, in contrast to the case for Fig. 5, these edges intersect the vertical coordinate planes at significantly different heights above the horizontal coordinate plane. In particular, the edges that run along the "Target D" axes rise more slowly than do the edges running along the "Target μ_a" axes. This behavior is a significantly better approximation to the ideal result [i.e., $\mu_a(t)^i$ independent of $D(t)^m$] than is that in Fig. 5. The results shown in Fig. 6 further demonstrate that the introduction of constraints and weight-matrix scaling does not introduce appreciable nonlinearity into the relation between the target and medium properties. Neither do they produce any dependence of the reconstructed coefficients in either inclusion on the properties that were present, in the target medium, in the other inclusion. This is an indication that the NCM achieves ef-

TABLE IV
NUMERICAL VALUES FOR EACH OF THE SIX ACCURACY FEATURE INDICES CONSIDERED IN THIS REPORT (SEE TABLE II AND SECTION II-D) FOR BOTH RECOVERED OPTICAL PARAMETERS AND BOTH RECONSTRUCTION ALGORITHMS

Accuracy Feature	Spatial Location	Optical parameter	Reconstruction Algorithm	
			NDM	NCM
Qualitative spatial accuracy of optical parameter values	Global	μ_a	0.54 – 0.58	0.78 – 0.86
	Global	D	0.55 – 0.60	0.83 – 0.86
Quantitative accuracy (global)	Global	μ_a	0.97 – 1.00	0.78 –0.84
	Global	D	0.82 – 1.17	0.56 – 0.83
Temporal fidelity	Left, right–hand inclusions (one pixel in each)	μ_a, D	97.2 – 99.6%	
Inter–parameter crosstalk	Left, right–hand inclusions (one pixel in each)	μ_a	52.2, 51.6%	10.7, 12.5%
		D	42.5, 41.7%	8.9, 9.0%
Qualitative spatial accuracy of temporal information[a]	Left, right–hand inclusions (one pixel in each)	μ_a	0.54, 0.56	0.74, 0.71
		D	0.59, 0.62	0.83, 0.83
Quantitative temporal accuracy	Left–hand inclusion (all pixels)	μ_a	4.8 – 5.0	4.7 – 4.8
		D	1.8 – 3.0	0.9 – 2.4
	Right–hand inclusion (all pixels)	μ_a	3.4 – 4.7	3.0 – 4.5
		D	0.4 – 3.1	0.3 – 4.4

a) Numbers in this row are computed values of the spatial correlation coefficient defined in the fifth row of Table II

fectively complete resolution of both the spatial and temporal contrast of the two inclusions.

D. Interparameter Crosstalk

The results displayed in the preceding figures are graphical demonstrations of the presence of interparameter crosstalk in the reconstructed μ_a time series, and of the fact that this feature is present to a smaller degree in the NCM results.

The crosstalk index values computed for the data that are plotted in Fig. 5 (NDM reconstruction) are $100r^2_{u'v}(L) = 52.2\%$, $100r^2_{u'v}(R) = 51.6\%$. The corresponding crosstalk indexes the NCM results (Fig. 6) are $100r^2_{u'v}(L) = 10.7\%$, $100r^2_{u'v}(R) = 12.5\%$. Recall that both algorithms gave temporal fidelity index values of nearly 100%. Taken together, the fidelity and crosstalk numbers show that when the NDM is used for image reconstruction, only somewhat less than half of the variability in $\mu_a(t)^i$ in the pixels considered here is linearly attributable to the variability that actually was present in $\mu_a(t)^m$. That is, the apparent μ_a reconstructed by the NDM is in reality essentially a 50/50 mixture of the target medium's μ_a and D. This is the worst-case scenario for interparameter crosstalk. On the other hand, when the NCM is used, approximately 90% of the variability in $\mu_a(t)^i$ is linearly attributable to the true variability of $\mu_a(t)^m$. This shift to a ~90/10 split indicates that the NCM achieves significant reductions in interparameter crosstalk, in addition to the already-noted improved spatial resolution.

If we now re-examine the data presented Fig. 4(B), we see that the NCM data yield larger CVs than the NDM data do in the $r_{u'v}$ time courses. In retrospect, this fact can be interpreted as an indirect suggestion that the former algorithm produces images containing less interparameter crosstalk. The reasoning underlying this conclusion is that u' is strongly correlated with v_{NDM} in both the spatial and temporal dimensions, but it is only in the spatial dimensions that u' is strongly correlated with v_{NCM}. Therefore, it can be expected that the $r_{u'v}$ time course corresponding to the NCM images will have a larger temporal vari-

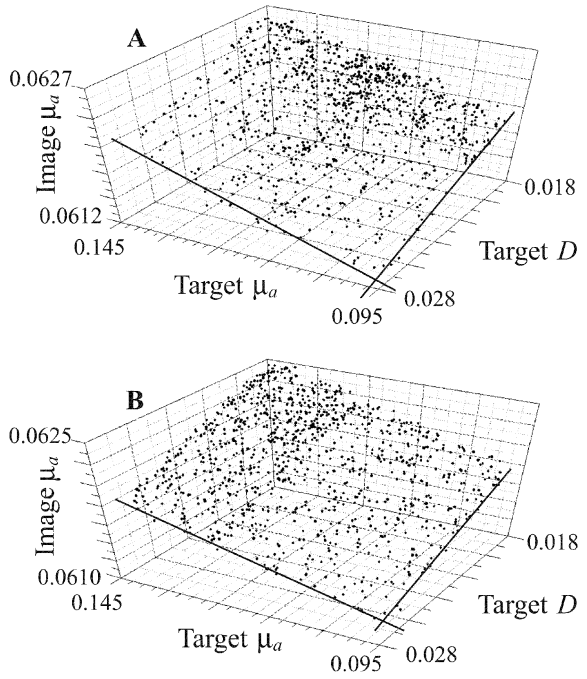

Fig. 5. Plots of μ_a reconstructed by using the NDM, versus modeled μ_a and D, for a selected pixel in (A) the left-hand and (B) right-hand inclusions. Each plotted point corresponds to a different time-point in the simulation time series. The surface defined by each set of plotted points is nearly planar. Pixels chosen for this display are those in (A) row 20, column 13 and (B) row 20, column 28 of the 40 × 40-pixel images (see Fig. 3).

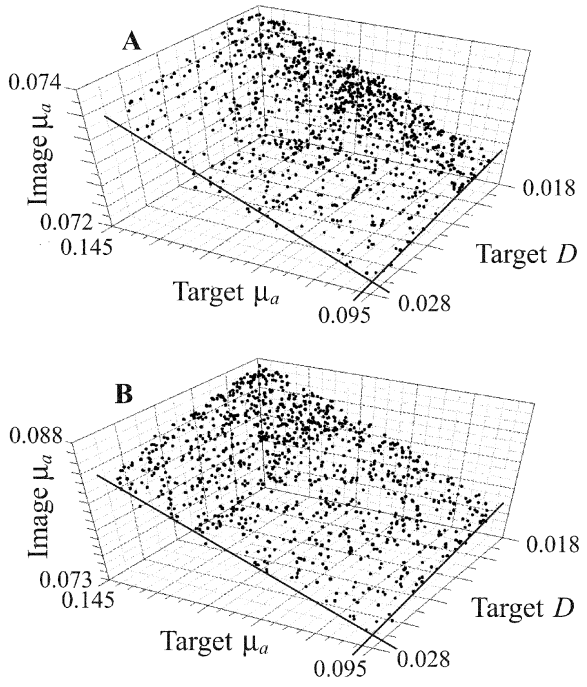

Fig. 6. Plots of μ_a reconstructed by using NCM versus modeled μ_a and D, for the same two pixels as were used for Fig. 5. Each plotted point corresponds to a different time-point in the simulation time series. The surface defined by each set of plotted points is nearly planar.

ance. The results of the single-pixel crosstalk index computations, however, provide a more definitive demonstration of the relative performance of the two algorithms with respect to this accuracy feature.

In order to achieve a more complete characterization of the spatial distribution of each modeled temporal function in the recovered images, we have looked for evidence of spatial crosstalk in the latter. This is quantified by using a percentage-of-variance index similar to that for interparameter crosstalk at a single location. The difference is that here the comparison is between the time series for a recovered optical parameter in a pixel within one inclusion and one or both of the functions assigned to the optical parameters of the other inclusion. Irrespective of the reconstruction algorithm, recovered parameter, or location within the images considered, the interinclusion crosstalk (a measure of spatial resolution) was never larger than 2.8%, and in most cases was less than 1%.

E. Qualitative Spatial Accuracy of Temporal Information

In Fig. 7, we show, for the results reconstructed by the NDM, maps of the standardized covariance between $\mu_a(t)^i$ and each of the four modeled functions $\mu_a(L, t)$, $D(L, t)$, $\mu_a(R, t)$, and $D(R, t)$. The dotted circles in each panel show the correct locations and sizes of the inclusions. The results in Fig. 7(A) and (B) indicate that both $\mu_a(L, t)$ and $\mu_a(R, t)$ are reproduced in the image time series in a spatially accurate manner. However, the data presented in Fig. 7(C) and (D) shows that $\mu_a(t)^i$ actually is a combination of $\mu_a(L, t)$ and $D(L, t)$ throughout the area of the left-hand inclusion, and of $\mu_a(R, t)$ and $D(R, t)$ throughout the area of the right-hand inclusion.

Analogous standardized covariance maps, computed from the $\mu_a(t)$ reconstructed by the NCM, are shown in Fig. 8. Here, we see [Fig. 8(A) and (B)] that the NCM also recovers the dynamic properties of the inclusions' absorption coefficients, with considerably better spatial accuracy. The maps shown in Fig. 8(C) and (D) indicate that interparameter crosstalk is not altogether eliminated by this algorithm. However, when the gray levels in Fig. 8(C) and (D) are contrasted with those in Fig. 8(A) and (B), it is apparent that the greatest (in absolute value) standardized covariance between $\mu_a(t)^i$ and either $D(L, t)$ or $D(R, t)$ is significantly smaller than that between $\mu_a(t)^i$ and either $\mu_a(L, t)$ or $\mu_a(R, t)$. This is a qualitatively better result than that of Fig. 7, in which the $\mu_a(t)^i$ versus $D(t)^m$ covariances are of the same magnitude as those between $\mu_a(t)^i$ and $\mu_a(t)^m$.

Just as for the static image data, spatial correlations between the ideal and observed spatial covariance maps can be meaningfully calculated for the data shown in panels (A) and (B) of Figs. 7 and 8. The ideal value is $+1$ in each case; the computed values for the data in Figs. 7(A), (B), and 8(A), (B) are 0.54, 0.56, 0.74, and 0.71, respectively. These numbers confirm the observation that the NCM yields higher spatial accuracy of temporal information.

A small degree of spatial crosstalk between the inclusions is evident in the results shown in Fig. 8. This is not an artifact specifically introduced by the NCM. Close examination of the corresponding results in Fig. 7 show that the same phenomenon is present in the NDM results, but is distributed over a larger area. This, and the greater variability in standardized covariance values found in the background region in the absence of constraints, renders the spatial crosstalk in the gray-scale images presented in Fig. 7 less noticeable than that in Fig. 8.

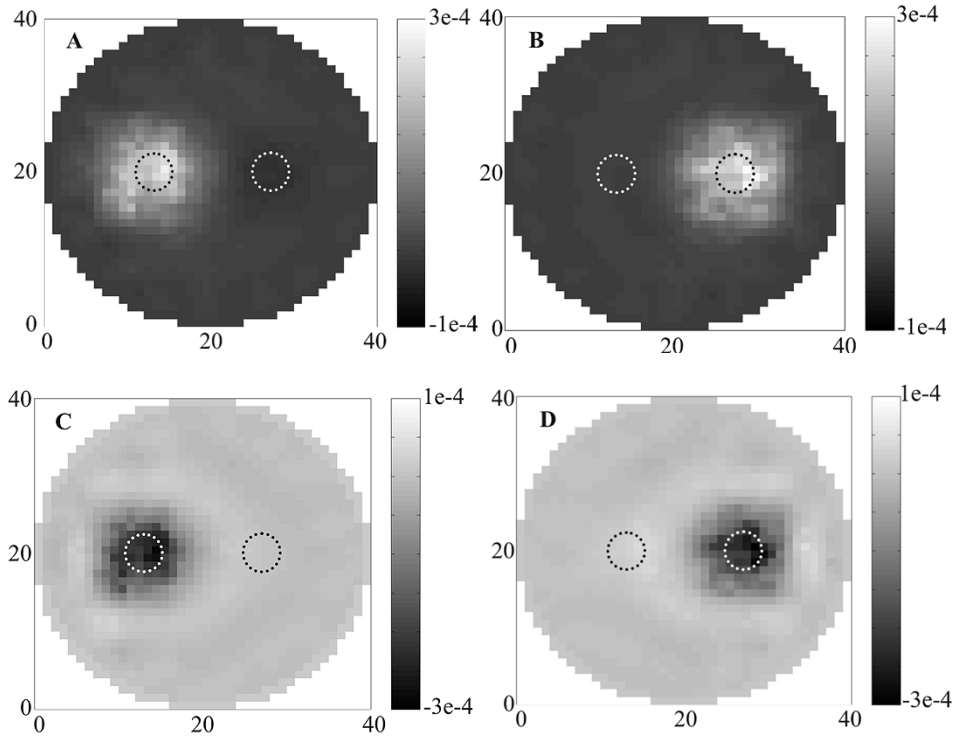

Fig. 7. Maps of standardized covariance (s^*_{uv}), in each pixel, between the μ_a image time series reconstructed by the NDM and each of the four temporal fluctuations that were present in the target medium. Plotted are s^*_{uv} between reconstructed μ^i_a and (A)$\mu_a(L,\ t)$, (B) $\mu_a(R,\ t)$, (C) $D(L,\ t)$, and (D) $D(R,\ t)$.

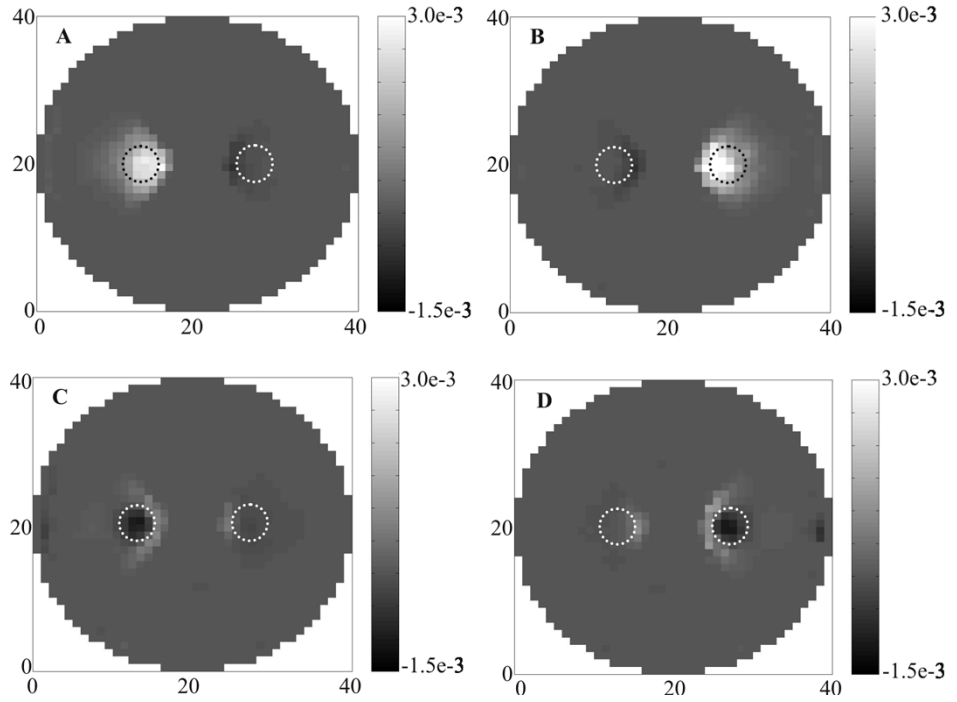

Fig. 8. Maps of standardized covariance (s^*_{uv}), in each pixel, between the μ_a image time series reconstructed by the NCM and each of the four temporal fluctuations that were present in the target medium. Plotted are s^*_{uv} between reconstructed μ_a and (A) $\mu_a(L,\ t)$, (B) $\mu_a(R,\ t)$, (C) $D(L,\ t)$, and (D) $D(R,\ t)$.

F. Quantitative Temporal Accuracy

As previously noted (see Section III-B above), the temporal mean value of the inclusions' μ_a was underestimated by both algorithms. It follows that quantitative accuracy of the recovered μ_a time series within the inclusions will be also be poor. (Outside the inclusions the target medium μ_a is constant, and so the quantitative temporal accuracy index in Table II is undefined.) For μ_a reconstructed by using the NDM, the quantitative temporal accuracy index is (mean, CV) 4.9, 0.5% for the left-hand inclusion, and 4.0, 10% for the right-hand inclusion. The indexes computed from the NCM data are left—4.7, 0.6%,

right—3.8, 13%. That is, there is no significant difference between the performance of the two algorithms with respect to the sixth accuracy feature.

Also noted previously is the fact that the quantitative accuracy of the temporal mean value of recovered D was greater than that of the recovered μ_a, for both algorithms. This pattern is seen as well in the quantitative accuracy indexes computed for the recovered D time series. These are: NDM, left—2.2, 13%; NDM, right—1.6, 52%; NCM, left—1.8, 25%; NCM, right—1.7, 61%. It is apparent that neither algorithm can quantitatively recover the coefficient values with the same degree of accuracy with which it can define the spatial location of the inclusions or their temporal properties.

G. Summary Tabulation of Results

While space limitations have led us to explicitly present image plots comparing only the reconstructed $\mu_a(t)$ to the temporal properties of the target medium (i.e., Figs. 3, 5–8), the corresponding analyses involving the reconstructed D time series also have been performed. The NCM yielded qualitatively superior $D(t)$ reconstructions than the NDM, of the same magnitude as those presented above for $\mu_a(t)$, in terms of both spatial resolution and interparameter crosstalk. The results of all temporal accuracy index computations, for time series of both recovered μ_a and D, are summarized in Table IV.

IV. Discussion and Conclusions

A. Review of Motivation

Optical imaging methods hold the promise of enabling the visualization of a range of functional properties of tissue that are not detectable using other imaging technologies. Their inherent sensitivity to hemoglobin, use of nonionizing energy sources, deep penetrating power in tissue, capacity to employ low-cost portable instrumentation, and recently added capability of monitoring dynamic states, all serve to underscore the expanding utility of this technology.

A series of recent reports have described instrumentation [1], [27], [28] and numerical methods [4], [29] that we have adopted for the collection and analysis of time-series image data. These methods represent various components of a more inclusive methodology that we seek to apply for the characterization of the spatiotemporal properties of hemoglobin states and vascular reactivity in large volumes of tissue using near infrared methods. It is our belief that such measures performed on tissue, either at rest or in response to some homeostatic provocation, represents a large untapped reservoir for identifying new diagnostic measures of disease processes, as well as for monitoring the influence of a host of therapeutic regimens.

While a number of reconstruction methods have been developed and many reports showing examples of recovered images have been published, there has so far been little emphasis placed on the need to specify quantitative criteria by which their performance can be measured and compared. With the introduction of an additional level of data-analysis complexity associated with performing dynamic measures [2]–[4], the necessity for objective quantitative indexes of image quality now is more pressing than previously. With reflection it quickly becomes apparent that the term "reconstruction accuracy" comprises many different aspects of the relation between medium and image. Thus, we chose to focus our attention on a limited number of specific properties that can be precisely defined, are quantifiable, and encompass among them most of the information that would be required for assessing the degree to which a reconstruction algorithm succeeds in reproducing the spatiotemporal structure of a target medium.

B. Significance of Reported Results

1) Qualitative Spatial Accuracy of Optical Parameter Images (Section III-A and Figs. 3 and 4): Perfect reconstruction results would have yielded values of $+1$ for r_{uv}, at all time points. As described, neither reconstruction algorithm achieved the ideal value, but both consistently gave significant positive r_{uv}s, and the performance of the NCM was markedly better than that of the NDM. Efforts to compare these numerical indexes of spatial accuracy to those in other reports, including some of our own, is hampered by their general absence in the literature.

We also observed that the CV associated with each r_{uv} is small ($<$2%) even though the true absorption and scattering coefficients varied by as much as $\pm$20%. We consider this an important observation, for the following reason. Suppose it were true that, as the most expansive interpretation possible of recent theoretical findings [37] would have it, a given set of detector data could correspond equally well to any spatial distribution of D. Then there is no reason why the spatial correlation between the target and image need be approximately equal at different instants in the time series. Thus, one might expect r_{uv} to take on all possible values between -1 and $+1$ with equal probability. The finding that r_{uv} actually exhibits little temporal variability (and is, besides, always greater than 0.5) implies that the phenomenon of nonunique correspondence between medium properties and detector readings is less problematical in practice than has sometimes been suggested.

2) Quantitative Accuracy of Static Optical Parameter Images (Section III-B): The results obtained for the target medium considered here would suggest that better quantitative accuracy is obtained when the NCM is used. In light of the finding that the NCM produces a more complete separation of the optical parameters, the quantitative results are not surprising. It bears repeating, however, that we assign higher priority to the goal of achieving high qualitative spatial and temporal accuracy, and that no particular effort was made to ensure good quantitative accuracy while developing the reconstruction methods that were compared here.

3) Temporal Fidelity (Section III-C, Figs. 5 and 6): Perhaps the most significant result obtained is the finding that both the NDM and NCM produce image time series that almost perfectly reproduce the local temporal behavior of the medium's optical parameters, in a spatially accurate manner. In the case of the NDM, while spatially local temporal properties are faithfully recovered, separation of two different temporally coincident signals [i.e., $\mu_a(t)$ and $D(t)$] was not possible. On the other hand, good separation of these parameters was achieved using the NCM, albeit, as noted above, not with any particular quantitative accuracy.

A corollary consideration stemming from our interest in examining the accuracy with which temporal behavior in optical properties can be recovered is that the added temporal dimension can serve as a useful diagnostic tool for both interparameter crosstalk and spatial blurring (i.e., the contribution of the medium's absorption or scattering contrast in one location to the value recovered in another location) arising from interactions among either local or nonlocal contrast features. In cases where blurring occurs in conjunction with local interparameter crosstalk, which we believe is the general case, it is hard to imagine how one could distinguish among these contaminating contrast features, or separate them from the true contrast recovered at any location, without some additional label. The analogy here is to the use of radioisotopes or other labels in imaging studies for the purpose of localizing and distinguishing specific features. Thus, the utility of considering temporal behavior in the optical coefficients extends beyond just its practical use as we have envisioned it.

One application we have considered, for which examination of temporal behavior could prove of particular value, is the specification of frequency-encoded spatial filters that can be used to improve image quality. The idea is analogous to the use of magnetic field gradients in MR imaging. For instance, suppose a medium has a different temporal frequency assigned to one of the optical parameters in each pixel. By examining the frequency spectrum of the recovered time series in each pixel, the contribution from each location in the target medium can be specified. This procedure, in effect, amounts to a simple one-step nonlinear correction. In practice, its utility would depend on the stability of the corresponding position-dependent frequency filter to the expected variability in a target medium.

It also deserves mention that the results obtained concerning the recovered temporal fidelity indexes reinforces the point made above regarding the issue of solution nonuniqueness. Given that each computation of temporal fidelity compares the properties of the medium and images at a single point, this accuracy feature should be a particularly sensitive indicator of any genuine inability of reconstruction methods that operate upon dc measurements to distinguish among different theoretically possible spatial distributions of optical parameters. The empirical observation that the temporal properties of the target were recovered with nearly perfect qualitative accuracy and in the correct location is a further indication that, as a practical matter, the existence of more than one medium corresponding to a given set of detector readings has little effect on the reliability of our recovered images.

4) Interparameter Crosstalk (Section III-D, Figs. 5 and 6): Results presented in this paper add to the evidence presented in recent studies by Pei *et al.*, [30], [31] wherein the NCM was first described and its ability to reduce interparameter crosstalk in dc imaging data was initially shown. Clearly demonstrated in this paper is the finding that the different test functions can be effectively isolated, irrespective of their functional form, or of the instantaneous value of the ratio of absorption to scatter.

It should be noted that, as was the case for spatial resolution, interparameter crosstalk is a concern common to all applications of optical tomography (i.e., not only for dynamic imaging). It is worth emphasizing that the correlation-based quantifications of these features that allowed for distinct specification of contrast from within and between both inclusions was possible because we reconstructed a time series of images from a medium exhibiting dynamic behavior. As mentioned above, the added temporal dimension allows for distinguishing among the sources of crosstalk.

C. Inverse Problem Solution Nonuniqueness

Recent attempts to disseminate findings such as those in this paper have been met with an increasing level of incredulity. As a consequence, we feel obliged to take a step beyond simply observing that these data imply that the main result of [37] should not be interpreted to mean that separation of the effects of absorption and scattering when recovering images from dc measurement data is a practical impossibility. Here, we offer plausible explanations that may serve to reconcile discrepancies between our observations and theoretical expectations.

In [37], an equation is derived that produces, for any specified initial spatial distributions of D and μ_a, an infinite family of alternative media that would yield identical surface measurements. To amplify upon discussions in reports by Pei *et al.* [30], [31], we believe reconciliation between the apparent inconsistency of our empirical findings with theoretical expectations can be traced to a failure to consider the volume that this set of media occupies in (D, μ_a)-space. We contend that in the overwhelming majority of cases, after all the alternative media that are physically or biologically unreasonable have been eliminated, those that remain all lie an acceptably small distance from the original medium. We further contend that the minority of cases for which this is not true, although probably infinite in number, probably constitutes a "dust" (i.e., a 0-dimensional set of unconnected points, possessing zero volume [38]) in the overall (D, μ_a)-space. The latter contention implies that an arbitrarily chosen pair of spatial distributions of D and μ_a has zero probability of belonging to this set.

Careful examination of the formula that generates the measurement-preserving alternative media [37] reveals that many of them, while mathematically valid, have properties that immediately allow us to exclude them from consideration. The most obvious are those which are physically impossible, requiring that μ_a be either negative or infinitely large at one or more locations within the medium. Others are quantitatively unreasonable, containing numerical values for μ_a that are larger than any actually found in tissue. Yet others are qualitatively unreasonable, possessing spatial distributions of μ_a that are either literally or effectively (i.e., large variations on an unrealistically small spatial scale) discontinuous. Still more can be excluded because they possess features that are selected against by most of the regularization techniques that are typically incorporated into image reconstruction algorithms. (It bears emphasizing that these are used precisely because they constrain the available solution space to media that conform to reasonable expectations and/or to *a priori* knowledge gleaned from other techniques.) Finally, an entire class of alternative media can, as a practical matter, be excluded because of the structure

that the objective function (i.e., the quantity that a reconstruction algorithm seeks to minimize) can be expected to have in the vicinity of these media. Namely, that the objective function increases rapidly with increasing distance from the point in the (D, μ_a)-space that corresponds to the alternative medium. This occurs because small changes in the spatial distribution of the alternative medium's optical properties are sufficient to produce appreciable changes in the surface detector readings, or, equivalently, in the value of the objective function. (It is interesting that the very example employed to illustrate the main result in [37] is of this type.) Consequently, an image reconstruction algorithm could produce one of these alternative solutions only if the initial guess supplied to the algorithm differed very little from said solution. That is, each of the alternatives in this class effectively corresponds to a singularity in the objective function.

Our experience with image reconstructions based on dc measurements (this paper and [30] and [31]) strongly suggests that after all the just-described unreasonable and effectively singular alternative media have been excluded, most of those that remain have the property that their spatial distributions of D and μ_a are qualitatively similar to those of the original medium. Within the space of all possible (D, μ_a) distribution pairs, these remaining alternatives lie within a bounded finite region that surrounds the point corresponding to the original medium. The results we have obtained lead us to conclude that in the ordinary course of events, the maximum radius of said region is sufficiently small that none of the alternative media within it differ from the original medium in a qualitatively significant manner.

We fully expect that with sufficient effort, exceptions to the preceding observational conclusion can be found; we will suppose for argument's sake that infinitely many such media exist. These have the property that after all unreasonable and effectively singular alternatives are excluded, those that remain still are distributed throughout the entire biologically feasible region of (D, μ_a)-space. The empirical fact is that we have not encountered any example of this latter type of medium, although there has been no particular effort on our part to avoid them. This leads us to advance the conjecture that these "pathological" media, while infinite in number, do not constitute a set with finite volume in (D, μ_a)-space. Rather, they correspond to a dust of isolated points, and the probability that an arbitrarily specified medium, or one composed of biological tissue, will happen to have exactly the spatial distributions of D and μ_a of one of these points is vanishingly small.

REFERENCES

[1] C. H. Schmitz, H. L. Graber, H. Luo, I. Arif, J. Hira, Y. Pei, A. Bluestone, S. Zhong, R. Andronica, I. Soller, N. Ramirez, S.-L. S. Barbour, and R. L. Barbour, "Instrumentation and calibration protocol for imaging dynamic features in dense-scattering media by optical tomography," *Appl. Opt.*, vol. 39, pp. 6466–6486, 2000.

[2] R. L. Barbour, H. L. Graber, C. H. Schmitz, Y. Pei, S. Zhong, S.-L. S. Barbour, S. Blattman, and T. Panetta, "Spatiotemporal imaging of vascular reactivity by optical tomography," in *Proceedings of Inter-Institute Workshop on In Vivo Optical Imaging at the NIH*, A. H. Gandjbakhche, Ed. Washington, DC: Opt. Soc. Amer., 2000, pp. 161–166.

[3] H. L. Graber, C. H. Schmitz, Y. Pei, S. Zhong, S.-L. S. Barbour, S. Blattman, T. Panetta, and R. L. Barbour, "Spatio–temporal imaging of vascular reactivity," in *Proc. SPIE*, C.-T. Chen and A. V. Clough, Eds., 2000, vol. 3978, Medical Imaging 2000: Physiology and Function from Multidimensional Images, pp. 364–376.

[4] R. L. Barbour, H. L. Graber, Y. Pei, S. Zhong, and C. H. Schmitz, "Optical tomographic imaging of dynamic features of dense-scattering media," *J. Opt. Soc. Amer. A*, vol. 19, pp. 3019–3036, 2001.

[5] B. Chance, R. R. Alfano, B. J. Tromberg, M. Tamura, and E. M. Sevick-Muraca, Eds., "Optical tomography and spectroscopy of tissue IV," *Proc. SPIE*, vol. 4250, 2001.

[6] M. Firbank, C. E. Elwell, C. E. Cooper, and D. T. Delpy, "Experimental and theoretical comparison on NIR spectroscopy measurements of cerebral hemoglobin changes," *J. Appl. Physiol.*, vol. 85, pp. 1915–1021, 1998.

[7] Y. Nomura, A. Matsunaga, and M. Tamura, "Optical characterization of heme $a + a_3$ and copper of cytochrome oxidase in blood-free perfused rat brain," *J. Neurosci. Meth.*, vol. 82, pp. 135–144, 1998.

[8] A. J. Fallgatter and W. K. Strik, "Right frontal activation during the continuous performance test assessed with near-infrared spectroscopy in healthy subjects," *Neurosci. Lett.*, vol. 223, pp. 89–92, 1997.

[9] H. Obrig, R. Wenzel, M. Kohl, S. Horst, P. Wobst, J. Steinbrink, F. Thomas, and A. Villringer, "Near-infrared spectroscopy: Does it function in functional activation studies in the human brain?," *Int. J. Psychophysiol.*, vol. 35, pp. 125–142, 2000.

[10] A. Zourabian, A. Siegel, B. Chance, N. Ramanujan, M. Rode, and D. A. Boas, "Trans-abdominal monitoring of fetal arterial blood oxygenation using pulse oximetry," *J. Biomed. Opt.*, vol. 5, pp. 391–405, 2000.

[11] G. Gratton, M. Fabiani, P. M. Corballis, D. C. Hood, M. R. Goodman-Wood, J. Hirsch, K. Kim, D. Friedman, and E. Gratton, "Fast and localized event-related optical signals (EROS) in the human occipital cortex: Comparisons with the visual evoked potential and fMRI," *Neuroimage*, vol. 6, pp. 168–180, 1997.

[12] B. Chance, Q. Luo, S. Nioka, D. C. Alsop, and J. A. Detre, "Optical investigations of physiology: A study of intrinsic and extrinsic biomedical contrast," *Philosophical Trans. Roy. Soc. London B*, vol. 352, pp. 707–716, 1997.

[13] G. R. Poe, D. A. Nitz, D. M. Rector, M. P. Kristensen, and R. M. Harper, "Concurrent reflectance imaging and microdialysis in the freely behaving cat," *J. Neurosci. Meth.*, vol. 65, pp. 143–149, 1996.

[14] J. Mayhew, Y. Zheng, Y. Hou, B. Vuksanovic, J. Berwick, S. Askew, and P. Coffey, "Spectroscopic analysis of changes in remitted illumination: the responses to increased neural activity in the brain," *Neuroimage*, vol. 10, pp. 304–326, 1999.

[15] M. A. Franceschini, V. Toronov, M. E. Filiaci, E. Gratton, and S. Fantini, "On-line optical imaging of the human brain with 160-ms temporal resolution," *Opt. Express*, vol. 6, pp. 49–57, 2000.

[16] A. Y. Bluestone, G. Abdoulaev, C. H. Schmitz, R. L. Barbour, and A. H. Hielscher, "Three-dimensional optical tomography of hemodynamics in the human head," *Opt. Express*, vol. 9, pp. 272–286, 2001.

[17] B. W. Pogue, S. P. Poplack, T. O. McBride, W. A. Wells, K. S. Osterman, U. L. Osterberg, and K. D. Paulsen, "Quantitative hemoglobin tomography with diffuse near-infrared spectroscopy: Pilot results in the breast," *Radiology*, vol. 218, pp. 261–266, 2001.

[18] Y. Xu, N. Iftimia, H. Jiang, L. L. Key, and M. B. Bolster, "Imaging of *in vitro* and *in vivo* bones and joints with continuous-wave diffuse optical tomography," *Opt. Express*, vol. 8, pp. 447–451, 2001.

[19] D. Contini, H. Liszka, A. Sassaroli, and G. Zaccanti, "Imaging of highly turbid media by the absorption method," *Appl. Opt.*, vol. 35, pp. 2315–2324, 1996.

[20] H. R. Heekeren, R. Wenzel, H. Obrig, J. Ruben, J.-P. Ndayisaba, Q. Luo, A. Dale, S. Nioka, M. Kohl, U. Dirnagl, A. Villringer, and B. Chance, "Toward noninvasve optical human brain mapping—Improvements of the spectral, temporal and spatial resolution of near-infrared spectroscopy," in *Proc. SPIE*, B. Chance and R. R. Alfano, Eds., 1997, vol. 2979, Optical Tomography and Spectroscopy of Tissue: Theory, Instrumentation, Model, and Human Studies II, pp. 847–857.

[21] H. Wabnitz and H. Winneberg, "Imaging in turbid media by photon density waves: spatial resolution and scaling relations," *Appl. Opt.*, vol. 36, pp. 64–74, 1997.

[22] D. J. Hall, J. C. Hebden, and D. T. Delpy, "Evaluation of spatial resolution as a function of thickness for time-resolved optical imaging of highly scattering media," *Med. Phys.*, vol. 24, pp. 361–368, 1997.

[23] R. Flewelling, "Noninvasive optical monitoring," in *The Biomedical Engineering Handbook*, 2nd ed, J. D. Bronzino, Ed. Boca Raton, FL: CRC, 2000, ch. 86.

[24] G. Drzewiecki, "Noninvasive arterial blood pressure and mechanics," in *The Biomedical Engineering Handbook*, 2nd ed, J. D. Bronzino, Ed. Boca Raton, FL: CRC, 2000, ch. 71.

[25] A. A. Shoukas and C. F. Rothe, "The venous system," in *The Biomedical Engineering Handbook*, 2nd ed, J. D. Bronzino, Ed. Boca Raton, FL: CRC, 2000, ch. 33.

[26] F. Deriu, S. Roatta, C. Grassi, R. Urciuoli, G. Micieli, and M. Passatore, "Sympathetically-induced changes in microvascular cerebral blood flow and in the morphology of its low-frequency waves," *J. Autonom. Nervous Syst.*, vol. 59, pp. 66–74, 1996.

[27] C. H. Schmitz, M. Löcker, J. Lasker, A. H. Hielscher, and R. L. Barbour, "Performance characteristics of a silicon photodiode (SiPD) based instrument for fast functional optical tomography," in *Proc. SPIE*, B. Chance, R. R. Alfano, B. J. Tromberg, M. Tamura, and E. M. Sevick-Muraca, Eds., 2001, vol. 4250, Optical Tomography and Spectroscopy of Tissue IV, pp. 171–179.

[28] ——, "Instrumentation for fast functional optical tomography," *Rev. Scientific Instrum.*, vol. 73, pp. 429–439, 2002.

[29] Y. Pei, H. L. Graber, and R. L. Barbour, "Influence of systematic errors in reference states on image quality and on stability of derived information for dc optical imaging," *Appl. Opt.*, vol. 40, pp. 5755–5769, 2001.

[30] ——, "Normalized-constraint method for minimizing inter-parameter crosstalk in reconstructed images of spatially heterogeneous scattering and absorption coefficients," in *Pro. SPIE*, B. Chance, R. R. Alfano, B. J. Tromberg, M. Tamura, and E. M. Sevick-Muraca, Eds., 2001, vol. 4250, Optical Tomography and Spectroscopy of Tissue IV, pp. 20–28.

[31] ——, "Normalized-constraint algorithm for minimizing inter-parameter crosstalk in dc optical tomography," *Opt. Express*, vol. 9, pp. 97–109, 2001.

[32] T. M. Griffith, "Chaos and fractals in vascular biology," *Vascular Med. Rev.*, vol. 5, pp. 161–182, 1994.

[33] A. H. Nayfeh and B. Balachandran, *Applied Nonlinear Dynamics: Analytical, Computational, and Experimental Methods*. New York: Wiley, 1995, ch. 4.

[34] K. Briggs, "An improved method for estimating Liapunov exponents of chaotic time series," *Phys. Lett. A*, vol. 151, pp. 27–32, 1990.

[35] R. L. Barbour, H. L. Graber, J. Chang, S.-L. S. Barbour, P. C. Koo, and R. Aronson, "MRI-guided optical tomography: Prospects and computation for a new imaging method," *IEEE Computat. Sci. Eng.*, vol. 2, no. 4, pp. 63–77, 1995.

[36] G. H. Golub and C. F. van Loan, *Matrix Computations*, 3rd ed. Baltimore, MD: Johns Hopkins Univ. Press, 1996, sec. 2.6.

[37] S. R. Arridge and W. R. B. Lionheart, "Nonuniqueness in diffusion-based optical tomography," *Opt. Lett.*, vol. 23, pp. 882–884, 1998.

[38] B. B. Mandelbrot, *The Fractal Geometry of Nature*. New York: Freeman, 1983, pp. 74–82.